

# Biomimetic Mineralized Hydroxyapatite Nanofiber-Incorporated Methacrylated Gelatin Hydrogel with Improved Mechanical and Osteoinductive Performances for Bone Regeneration

He Wang <sup>1,\*</sup>, Bo Hu <sup>1,\*</sup>, Hong Li<sup>2</sup>, Ge Feng<sup>1</sup>, Shengyuan Pan<sup>1</sup>, Ziqi Chen <sup>1</sup>, Bo Li<sup>2</sup>, Jinlin Song <sup>1</sup>

<sup>1</sup>Stomatological Hospital of Chongqing Medical University, Chongqing Key Laboratory of Oral Diseases and Biomedical Sciences, Chongqing Municipal Key Laboratory of Oral Biomedical Engineering of Higher Education, Chongqing, People's Republic of China; <sup>2</sup>Chongqing Engineering Laboratory of Nano/Micro Biomedical Detection Technology, Chongqing University of Science and Technology, Chongqing, People's Republic of China

\*These authors contributed equally to this work

Correspondence: Bo Li, Chongqing Engineering Laboratory of Nano/Micro Biomedical Detection Technology, Chongqing University of Science and Technology, Chongqing, 401331, People's Republic of China, Tel +86-23-8886-0026, Fax +86-23-8886-0222, Email Libo@cqust.edu.cn; Jinlin Song, College of Stomatology, Chongqing Medical University, 426# Songshibei Road, Yubei District, Chongqing, 401147, People's Republic of China, Tel +86-23-8886-0026, Fax +86-23-8886-0222, Email songjinlin@hospital.cqmu.edu.cn

**Purpose:** Methacrylic anhydride-modified gelatin (GelMA) hydrogels exhibit many beneficial biological features and are widely studied for bone tissue regeneration. However, deficiencies in the mechanical strength, osteogenic factors and mineral ions limit their application in bone defect regeneration. Incorporation of inorganic fillers into GelMA to improve its mechanical properties and bone regenerative ability has been one of the research hotspots.

**Methods:** In this work, hydroxyapatite nanofibers (HANFs) were prepared and mineralized in a simulated body fluid to make their components and structure more similar to those of natural bone apatite, and then different amounts of mineralized HANFs (m-HANFs) were incorporated into the GelMA hydrogel to form m-HANFs/GelMA composite hydrogels. The physicochemical properties, biocompatibility and bone regenerative ability of m-HANFs/GelMA were determined in vitro and in vivo.

**Results:** The results indicated that m-HANFs with high aspect ratio presented rough and porous surfaces coated with bone-like apatite crystals. The incorporation of biomimetic m-HANFs improved the biocompatibility, mechanical, swelling, degradation and bone regenerative performances of GelMA. However, the improvement in the performance of the composite hydrogel did not continuously increase as the amount of added m-HANFs increased, and the 15m-HANFs/GelMA group exhibited the best swelling and degradation performances and the best bone repair effect in vivo among all the groups.

**Conclusion:** The biomimetic m-HANFs/GelMA composite hydrogel can provide a novel option for bone tissue engineering in the future; however, it needs further investigations to optimize the proportions of m-HANFs and GelMA for improving the bone repair effect.

**Keywords:** biomimetic composite hydrogel, mineralized hydroxyapatite nanofiber, GelMA, bone regeneration

## Introduction

Tissue engineering holds great promise in regenerating bone defects of large volumes.<sup>1</sup> Scaffolds serve as templates for bone regeneration while providing a matrix for cellular support and are known to be one of the three essential factors involved in bone tissue engineering.<sup>2,3</sup> An ideal bone tissue engineering scaffold should be biocompatible, highly porous and biodegradable, with good osteogenic inductive activities, and its mechanical properties should match those of host bone tissues.<sup>4,5</sup>

Hydrogels, such as those of natural and synthetic polymers,<sup>6</sup> have been widely used in tissue engineering because they can be easily formed and processed. More importantly, their microstructures are similar to that of the natural extracellular

microenvironment, which is favorable for cell growth and tissue regeneration.<sup>7,8</sup> Polysaccharide-type natural polymers, such as hyaluronate,<sup>9</sup> alginate and chitosan,<sup>10,11</sup> protein-type natural polymers, such as gelatin and collagen,<sup>12,13</sup> and synthetic polymers, such as poly(N-isopropylacrylamide) and poly(ethylene glycol),<sup>14,15</sup> have all been well studied. In particular, gelatin is a collagen derivative with many beneficial biological features, such as the matrix metalloproteinase (MMP)-sensitive degradation sites and the Arg-Gly-Asp (RGD) sequence, which facilitates cell migration, adhesion and differentiation.<sup>16</sup> Methacrylic anhydride-modified gelatin (GelMA) is a modified gelatin grafted with methacrylic anhydride and inherits the aforementioned molecular characteristics from collagen.<sup>17,18</sup> GelMA can be easily used to prepare hydrogels by a chemical crosslinking or photocrosslinking method. However, the lack of mechanical strength and mineral ions such as calcium and phosphorus, which are essential for osteogenesis, limits the application of these hydrogels in the field of bone repair.<sup>19</sup> Therefore, enhancing the mechanical properties of these hydrogels to meet the requirements of bone regeneration has always been one of the research hotspots in bone tissue engineering.

Some researchers have modified hydrogels by incorporating different inorganic nanoparticles, such as hydroxyapatite (HA),<sup>20,21</sup> bioactive glass and  $\beta$ -tricalcium phosphate nanoparticles,<sup>22,23</sup> to improve the bone regeneration capacities of hydrogels. The results demonstrated that these fillers could, to some extent, change the hydrogel structure and improve its mechanical strength and osteoinductivity.<sup>24,25</sup> However, the effect of nanoscale particle fillers on increasing the mechanical strength of materials is limited when they are added at a relatively low level. Moreover, it is difficult for nanoscale particles to achieve a homogeneous dispersion in a polymeric matrix, especially when the amount of the filler added is increased to a relatively high level, because excess fillers tend to agglomerate, and this has a negative impact on the mechanical properties of the resulting substrates and may affect the final osteogenic effect.<sup>26</sup> Therefore, one-dimensional bioceramic fillers with high aspect ratios are considered more promising reinforcements in this context, owing to their better supporting effect with ability to bridge and form networks.<sup>27</sup> To date, many one-dimensional fillers, such as HA nanofibers (HANFs),<sup>28</sup> glass fibers and halloysite nanotubes,<sup>29,30</sup> have been used to strengthen materials and develop bone grafts and cements with a higher bone regenerative capacity. Among them, HANFs, a synthetic inorganic material with a chemical composition similar to that of biological bone tissue, can confer an enhanced biological activity and mechanical performance to GelMA.<sup>31</sup> However, traditionally synthesized HANFs are HA crystals that preferentially grow along the c-axis,<sup>32</sup> which is a property that differs from those of natural bone tissues in organisms.<sup>33</sup> The inorganic phase of natural bone tissues is mostly bone-like apatite with a low degree of crystallization.<sup>34</sup> It can constantly release calcium ( $\text{Ca}^{2+}$ ) and phosphate ( $\text{PO}_4^{3-}$ ) ions, which have a great influence on the bone mineralization process. Therefore, it is critical to further modify the HANFs to make them more biomimetic and similar to natural bone tissues. However, so far no published studies have tried to utilize biomimetically modified HANFs to enhance GelMA to improve its bone regenerative capacity.

Therefore, in this study, we successfully prepared HANFs with ultrahigh aspect ratio and mineralized them in a simulated body fluid (SBF) to make their surfaces coated with a layer of bone-like apatite. The trace element doped biomimetic apatite mineral layer on the mineralized HANFs' (m-HANFs) surfaces simulated the natural bone apatite in structure and composition and was beneficial for bone regeneration. Then, different amounts of m-HANFs were incorporated into GelMA to form m-HANFs/GelMA composite hydrogels. We determined the physicochemical properties, biocompatibility and bone regenerative effect of these composite hydrogels in vitro and in vivo and preliminarily explored the optimal amount of m-HANF addition to promote bone regeneration, in order to provide a theoretical basis for the application of m-HANFs/GelMA composite hydrogels in bone tissue engineering in the future (Figure 1).

## Materials and Methods

### Materials

Calcium chloride ( $\text{CaCl}_2$ ), sodium dihydrogen phosphate ( $\text{NaH}_2\text{PO}_4$ ), sodium hydroxide (NaOH), oleic acid, anhydrous ethanol and phosphate buffer (PBS) were obtained from Chengdu Kelong Chemical Co., Ltd. (Chengdu, Sichuan, China). Gelatin, methacrylic anhydride, ammonium persulfate (APS) and tetramethylethylenediamine (TEMED) were purchased from Aladdin Reagent Company (Shanghai, China). Fetal bovine serum (FBS) and  $\alpha$ -Minimum Essential Medium ( $\alpha$ -MEM) were purchased from Gibco (Grand Island, NY, USA). Streptomycin, penicillin and trypsin were purchased from

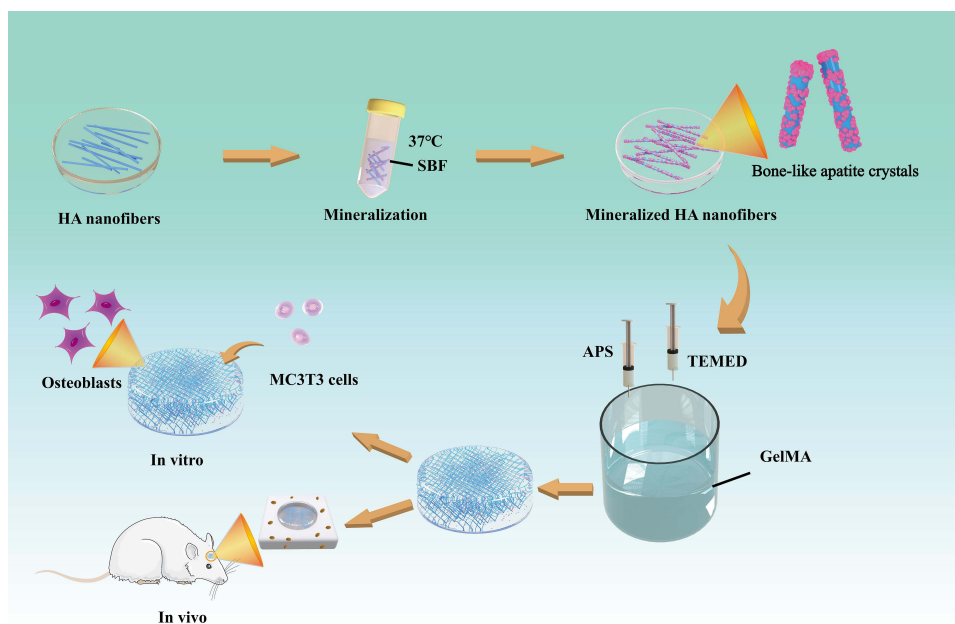


**Figure 1** Fabrication of m-HANFs/GelMA hydrogels for the advancement of osteogenic differentiation of MC3T3 cells in vitro and bone formation in vivo.

Biosharp (Anhui, China). Dexamethasone, ascorbic acid-2 phosphate and  $\beta$ -glycerophosphate were purchased from Beijing Solarbio Sciences Co. (Beijing, China). Mouse calvaria-derived (subclone 14) osteoblast-like cells (MC3T3-E1) were purchased from Cobioer Co. (Nanjing, Jiangsu, China). The Sprague-Dawley rats used in this study were purchased from Chongqing Medical University Animal Care and Use Committee. All reagents were analytically pure and used as received. The experimental water was deionized water.

## Preparation of m-HANFs/GelMA Composite Hydrogels

### Mineralized Hydroxyapatite Nanofibers

HA nanofibers were prepared by a solvothermal method according to a previous report with some modifications.<sup>35</sup> In brief, the calcium oleate precursor was prepared first. Ten milliliters of a NaOH solution (0.5 g) was slowly added to an ethanol (6 g) and oleic acid (6 g) mixture with even mixing, and then 10 mL of a  $\text{CaCl}_2$  solution (0.11 g) and 5 mL of a  $\text{NaH}_2\text{PO}_4 \cdot 2\text{H}_2\text{O}$  solution (0.2 g) were added dropwise. The mixture was transferred to an autoclave at 180 °C for 23 h. The product was washed with ethanol and deionized water by centrifugation and then freeze-dried to produce HA nanofibers.

The as-prepared HA nanofibers were immersed in SBF to induce mineralization.<sup>36</sup> The HA nanofibers (20 mg) were dispersed in a 30 mL SBF solution, sealed in EP tubes (50 mL) and placed in a 37 °C incubator. After 1 day, 3 days and 5 days, the incubated HA fibers were removed and rinsed with deionized water. The mineralization of HA nanofibers was observed through scanning electron microscopy (SEM, JSM-7800F, JEOL, Japan). Finally, mineralized HA nanofibers (m-HANFs) were selected after 5 days for subsequent experiments.

### Methacrylic Anhydride-Modified Gelatin (GelMA)

GelMA was prepared according to our previous report.<sup>37</sup> Briefly, 5 g type A gelatin was dissolved in a 50 mL PBS solution with magnetic stirring at 50 °C. After the solution became transparent, 5 mL methacrylic anhydride was added dropwise. After 3 h of reaction, the mixture was diluted with 250 mL PBS and transferred to a dialysis tube (the molecular weight cutoff (MWCO) was 12,000–14,000 Da; VWR Scientific, USA) for dialysis against deionized water for 5 days at 60 °C to remove unreacted MA. After dialysis, the GelMA solution was further purified by centrifugation and then lyophilized (Lab-1D-80, BoYiKang, Beijing, China).

## m-HANFs/GelMA Composite Hydrogel

m-HANFs/GelMA composite hydrogels with different amounts of m-HANFs were prepared. Typically, 100 mg GelMA was dissolved in 1 mL PBS (ie, 10% by mass and volume), and 0 mg, 5 mg, 15 mg and 25 mg m-HANFs were added to the solution (Table 1). The mixture underwent an ultrasound treatment for 5 min to evenly mix the solutions. After 5 mg of APS and 2.5  $\mu$ L of TEMED were mixed in the solution, the mixture was rapidly transferred to a homemade resin mold to form the m-HANFs/GelMA hydrogel (Figure S1). The process of m-HANFs/GelMA hydrogel preparation is shown in Figure 1.

## Physical and Chemical Characterization

### Morphology and Phase Composition

The m-HANFs were dispersed in alcohol, dripped on a conductive adhesive, sprayed gold, and observed by a scanning electron microscope (JSM-7800F, JEOL, Japan). After being freeze-dried, the m-HANFs/GelMA was quenched in liquid nitrogen and cut apart. The cross section of the sample was observed through SEM. To observe the structure and distribution of m-HANFs inside the composite hydrogel, the 5, 15, and 25m-HANFs/GelMA composite hydrogel samples were scanned by Micro-CT (Scanco, Brüttisellen, Switzerland). The samples were ground into powder, and the phase composition was analyzed with X-ray diffraction (XRD, Smartlab-9, Rigaku, Japan) with Cu K $\alpha$  radiation. The XRD patterns were recorded at a rate of 2.0 $^{\circ}$ /min at 40 kV and 30 mA in the range of 2 $\theta$ =20–55 $^{\circ}$ .

### Mechanical Test

The mechanical properties of the composite hydrogel were characterized by stress-strain curves. A cylindrical hydrogel sample with a diameter of approximately 8.50 mm and a thickness of approximately 3.50 mm was prepared. The hydrogel material was compressed in the axial direction using a universal mechanical test machine (CMT-1202, SUST Electrical Equipment, Zhuhai, China) with a 200 N load cell at a cross head rate of 1 mm/min, and the compression rate was reduced to 90% when the strain or fracture was stopped. A total of 10 samples were taken from each group for testing. The compressive modulus of the hydrogel was calculated utilizing the first 10% of the stress-strain curve of the sample, and the expression of the obtained elastic modulus is the mean value of the standard deviation.

### Swelling Property and Degradation Performance

The dry weight of the composite hydrogels was recorded after they were freeze-dried, and the hydrogels were then soaked in PBS at 37  $^{\circ}$ C. The composite hydrogels were removed at predetermined times, and the weights were recorded after the surface moisture was absorbed. There were 6 samples in each group. The swelling ratio of the m-HANFs/GelMA composite hydrogel under PBS conditions is as follows:

$$\text{Swelling ratio} = (W_1 - W_0) / W_0 \times 100\%$$

where  $W_0$  (g) is the mass after drying and  $W_1$  (g) is the mass after water absorption.

The composite hydrogels were freeze-dried and weighed. The dry composite was added to 7 mL of PBS and placed into a shaker (Figure S2). The temperature was set to 37  $^{\circ}$ C, and the rotation speed was 120 r/min. After the predetermined degradation time, the solution in the centrifuge tube was removed, and the sample was washed twice

**Table 1** Sample of m-HANFs/GelMA

No.	m-HANFS/mg	GelMA/mg	PBS/mL	APS/mg	TMEDA/ $\mu$ L	Mass Fraction/wt%
0m-HANFs/GelMA	0	100	1	5	2.5	0
5m-HANFs/GelMA	5	100	1	5	2.5	4.5
15m-HANFs/GelMA	15	100	1	5	2.5	12.5
25m-HANFs/GelMA	25	100	1	5	2.5	19.2

**Abbreviations:** PBS, phosphate buffer; APS, ammonium persulphate; TMEDA, N,N,N',N'-tetramethylethylenediamine.

with water. The sample was lyophilized, and the weight was recorded. The formula of the m-HANFs/GelMA hydrogel degradation rate in PBS is as follows:

$$\text{Degradation rate} = (W_0 - W) / W_0 \times 100\%$$

Where  $W_0$  (g) is the original weight after drying, and  $W$  (g) is the lyophilized weight after different times.

## In vitro Cell Culture and Cytocompatibility Investigation

MC3T3-E1 cells and rat bone marrow mesenchymal stem cells (rBMSCs) were cultured in 10 cm petri dishes with complete medium ( $\alpha$ MEM supplemented with 10% FBS, 100 mg/mL streptomycin and 100 U/mL penicillin) at 37 °C in a 5% CO<sub>2</sub> humidified incubator. The medium was replaced every 3 days. When the cells were 80% to 90% fused, they were digested with trypsin for subsequent use.

To quantitatively estimate the biocompatibility of our composite hydrogel, we conducted a cytotoxicity study with MC3T3-E1 cells and rBMSCs. The four groups of hydrogels (0, 5, 15, 25, n=5) were incubated with complete medium at 37 °C in a 5% CO<sub>2</sub> incubator for 24 h. The extract was collected and diluted with fresh complete medium. Confluent MC3T3-E1 cells and rBMSCs were trypsinized and seeded in a 96-well plate at  $1 \times 10^3$  cells/well and incubated for 24 h. After 24 h, the medium was replaced with diluted composite hydrogel extracts or fresh complete medium and incubated for 1, 3, 5 and 7 days. Cell viability was detected utilizing Cell Counting Kit-8 (CCK-8, Abcam, Cambridge, UK) at each timepoint. The absorption values were read with an automated microplate reader (Perkin Elmer, USA) at a wavelength of 450 nm. The experiment was repeated 3 times.

Next, the composite hydrogels (diameter 3 mm) were sterilized under UV light for 2 h, placed in a 48-well plate with 500  $\mu$ L complete medium and cocultured for 3 h. Then, the medium was aspirated, and MC3T3-E1 cell suspensions were seeded onto the composite hydrogel surfaces (n=5) at  $2 \times 10^4$  cells/sample. After 3 days of incubation, cells were treated with a calcein-AM/EthD1 double stain kit (Dojindo, Japan) and observed under a laser confocal scanning microscope (LCSM, Leica SP8, Germany). For SEM observation, cells were fixed with 2.5% glutaraldehyde for 4 h, followed by sequential dehydration in a graded series of ethanol (50, 70, 80, 90, 95 and 100 v/v%) for 10 min each. After the cells were freeze-dried, the MC3T3-E1 cell morphology of the four groups was observed utilizing SEM (Hitachi, Japan).

## In vitro Osteogenic Differentiation

To compare the in vitro cell osteoinductivity of the composite hydrogels, we performed alkaline phosphatase (ALP) and alizarin red staining. ALP is a glycoprotein expressed by osteoblasts and is a sensitive and reliable indicator of early bone differentiation. Alizarin red dye binds to Ca<sup>2+</sup>, one of the main inorganic components of bone. Four groups of composite hydrogels were placed in a 48-well plate and seeded with cells at  $2 \times 10^4$  cells/sample. After 24 h, the medium was replaced with osteogenic induction medium (complete medium with 50  $\mu$ g/mL ascorbic acid-2 phosphate, 10 mM  $\beta$ -glycerophosphate, and 10 nM dexamethasone) and cultured for 7 and 21 days. The medium was replaced every 3 days. All experiments were repeated three times.

### ALP Staining

After 7 days of culture, ALP staining was conducted following the ALP staining kit (Beyotime, Shanghai, China) instructions. Briefly, the samples were washed twice with PBS, fixed with 4% paraformaldehyde (PFA, Solarbio) for 30 min and washed twice with PBS again to remove the participating fixative, and correlated staining was performed according to the instructions. After being stained, the samples were observed under a light microscope, and images were captured with a stereo microscope (StereoDiscovery, Carl Zeiss, Germany). All experiments were repeated three times.

### Alizarin Red Staining

The calcium deposition from cells in the composite hydrogel was evaluated by alizarin red dye. After 21 days of culture, the samples were washed twice with PBS, fixed with 4% PFA for 30 min and washed again. Alizarin red solution (Solarbio, Beijing, China) was added to the well plates, and the plates were incubated for 30 min in the dark. After incubation, the samples were washed 3 times with deionized water. The plate was placed under the stereo microscope to obtain images. To quantify calcium deposition, the samples were stained with alizarin red then destained with 10%

cetylpyridinium chloride monohydrate (CPC, Solarbio, Beijing, China). The dissolved mixture ( $n = 5$ ) was then transferred to a 96-well plate, and the absorbance was measured at 402 nm by a microplate reader (Perkin Elmer, USA). All experiments were repeated 3 times.

## Repair Assay in the Rat Critical-Size Calvarial Defect Model

The animal experiments were approved by the Animal Experimental Ethics Committee of Stomatological Hospital of Chongqing Medical University (Permit Number: 2021057) and the animals were kept following the guidelines of the National Institutes of Health Guide for the Care and Use of Laboratory Animals (NIH Publications No. 8023, revised 1978). 6-week-old Sprague-Dawley rats ( $250 \pm 50$  g) were randomly distributed to the blank, 0, 5, 15 and 25m-HANFs/GelMA groups. After anesthesia was administered, each rat was shaved from the snout to the end of the calvarium, the skin was painted with iodine swabs, and an incision was made. Then, a surgical drill and trephine were used to create full-thickness critical-size calvarial defects (8 mm in diameter) under the irrigation of sterile normal saline. The defects were placed with different groups of composite hydrogels or left untreated. The periosteum and skin were closed separately with interrupted 3–0 nylon sutures. The animals were housed singly in cages at a constant temperature of  $23 \pm 3$  °C. Twelve weeks after the operation, the rats were euthanized by CO<sub>2</sub> asphyxiation, and then the calvarias were harvested and fixed in 10% (vol/vol) buffered formalin. Micro-CT scanning was conducted to evaluate the reparative efficacies of the implantations. The calvaria samples were decalcified with 10% EDTA for 2 months and then sectioned in the coronal plane for H&E, Masson trichrome, and immunohistochemistry (Runx2, Col1a1, OCN) staining.

## Statistical Analysis

The data are presented as the mean  $\pm$  standard deviation. One-way analysis of variance (ANOVA) was used to analyze the significant differences between samples. For all tests, the levels of significance were set to  $p < 0.05$ ,  $p < 0.01$ ,  $p < 0.001$  and  $p < 0.0001$ . All the data were statistically analyzed using GraphPad Prism 9.0.

## Results and Discussion

GelMA has been widely used for tissue engineering with cell-binding sequence RGD and MMP-sensitive degradation motifs.<sup>38,39</sup> Unfortunately, unmodified GelMA hydrogels degrade quickly, lack mechanical integrity, and, most importantly, lack calcium and phosphorus needed in the osteogenic process; therefore, the application of these hydrogels in the field of bone regeneration is limited. The combination of bioceramic materials and hydrogels to form composites with better osteogenic ability for the repair of bone defects has long been a hotspot of research.

Nanoscale particle fillers, like hydroxyapatite nanoparticles (HANPs) are widely used to reinforce hydrogel in the field of bone tissue engineering, in spite of the fact that their effect on increasing the mechanical strength of the hydrogel is limited. By contrast, HANFs with super aspect ratio can provide stronger reinforcements for the hydrogel owing to their better supporting effect with ability to bridge and form networks.<sup>27</sup> Moreover, traditionally synthesized HA are HA crystals that preferentially grow along the *c*-axis,<sup>32</sup> which is a property that differs from those of natural bone tissues.<sup>33</sup> Therefore, it is critical to further modify HANFs to make their structure and components more similar to those of natural bone tissues and then incorporate them into GelMA to endow it with better bone regenerative ability. However, so far no published studies have utilized biomimetically modified HANFs to enhance GelMA with improved bone regenerative capacity. Moreover, as observed by other authors, the physicochemical properties and osteogenic ability of the composite hydrogel could be greatly affected by the amounts of bioceramic materials incorporated,<sup>40,41</sup> which, however, might not follow a proportionate trend as the amounts of added fillers increased.<sup>42</sup>

Therefore, in this study, a biomimetic m-HANFs incorporated GelMA hydrogel was successfully developed. We determined the physicochemical properties, biocompatibility and bone regenerative effect of these composite hydrogels *in vitro* and *in vivo* and preliminarily explored the optimal amount of m-HANF addition to promote bone regenerative efficiency, in order to provide a theoretical basis for the application of m-HANFs/GelMA composite hydrogels in bone tissue engineering in the future.

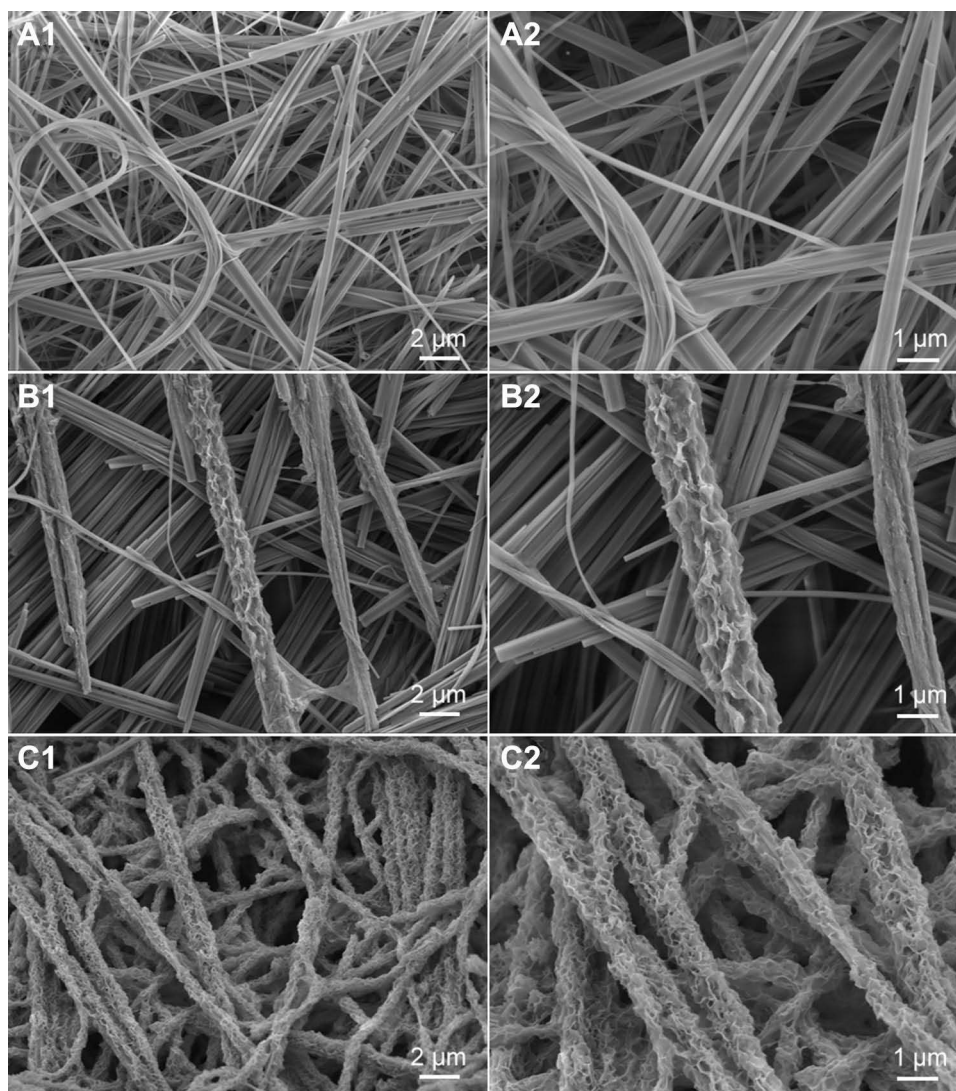


**Figure 2** SEM images of HANFs that were mineralized for 0 d (**A1** and **A2**), 3 d (**B1** and **B2**) and 5 d (**C1** and **C2**).

## Morphology and Phase Composition

**Figure 2** shows the SEM images of HA nanofibers and mineralized HA nanofibers after they were immersed in SBF for different times. The HA nanofibers prepared by the solvothermal method clearly had lengths that were too long to be accurately measured by SEM and had an ultrahigh aspect ratio (**Figure 2A1** and **A2**). On the one hand, with time increasing from 0 to 5 days (**Figure 2A–C**), it could be clearly found that the diameter of nanofiber increased significantly. On the other hand, as the mineralization time increased from 0 to 3 days (**Figure 2A** and **B**), an increasing number of flower-like minerals were formed on the surface of the HA nanofibers. After 5 days (**Figure 2C1** and **C2**), all their surfaces were covered by flower-like minerals with regular shape. SBF is a solution highly supersaturated with respect to apatite, which contains abundant ions such as  $\text{PO}_4^{3-}$ ,  $\text{Ca}^{2+}$  and  $\text{CO}_3^{2-}$ . When HANFs were immersed in SBF, the  $\text{PO}_4^{3-}$ ,  $\text{Ca}^{2+}$  and some oleic acid molecule from HANFs could induce the deposition of  $\text{PO}_4^{3-}$ ,  $\text{Ca}^{2+}$  and  $\text{CO}_3^{2-}$  from SBF onto the surface of HANFs to form flower-like apatite crystals with regular shape.<sup>36</sup> So it could be concluded that the  $\text{PO}_4^{3-}$ ,  $\text{Ca}^{2+}$ ,  $\text{CO}_3^{2-}$  and other ions from SBF could be also incorporated into the flower-like apatite crystals. This trace element doped flower-like apatite mineral layer simulated the natural bone apatite in structure and composition, which was beneficial for bone regeneration.<sup>36</sup> Moreover, the surfaces of m-HANFs became rougher and more porous after mineralization. More enhanced cell adhesion and tissue ingrowth can occur with rough implant surfaces than with

smooth surfaces.<sup>43,44</sup> Therefore, we successfully prepared m-HANFs with super aspect ratio, and after 5 days of mineralization, the m-HANFs coated with biomimetic apatite were incorporated into GelMA to prepare composite hydrogels for subsequent experiments.

Figure 3 shows the cross-sectional images of pure GelMA and m-HANFs/GelMA composite hydrogels, and the m-HANFs were mixed homogeneously within the GelMA matrix. All m-HANFs/GelMA hydrogels had a loose network

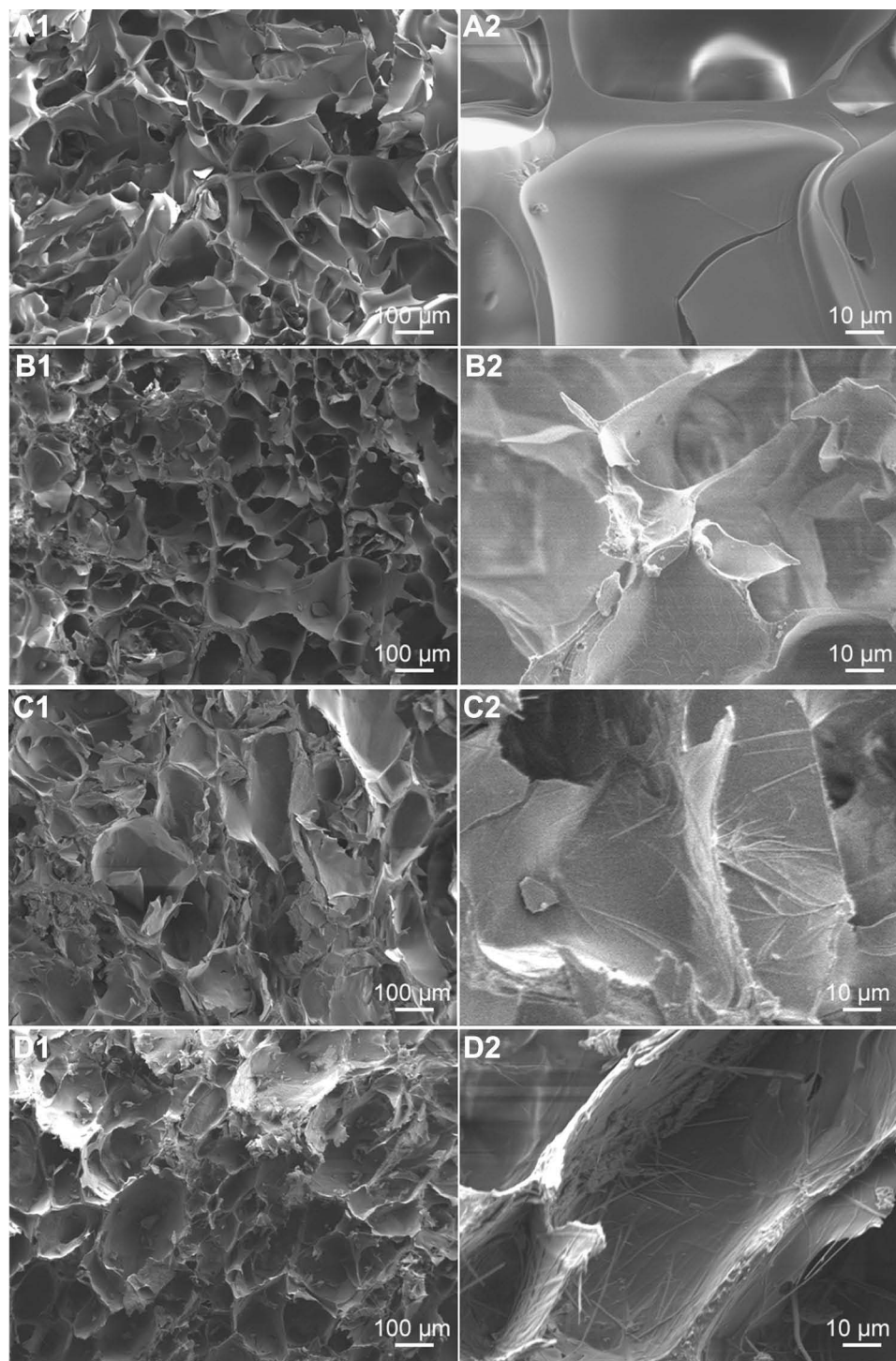


**Figure 3** SEM images of 0m-HANFs/GelMA (**A1** and **A2**), 5m-HANFs/GelMA (**B1** and **B2**), 15m-HANFs/GelMA (**C1** and **C2**) and 25m-HANFs/GelMA (**D1** and **D2**) composite hydrogels.

porous structure with a pore size of approximately 100  $\mu\text{m}$  regardless of the amount of m-HANFs added, which suggested that the addition of m-HANFs had little effect on the pore size of the GelMA hydrogel; this structure thus contributed to the retention of large amounts of water and further promoted diffusion of nutrients and macromolecules inside the GelMA matrix.<sup>41,45</sup> With the increase in the mass fraction of m-HANFs, the m-HANFs in the pore wall of the hydrogel increased significantly, which might provide the foundation for energy dissipation that enhanced the mechanical properties and increased cell adhesion at the same time.

Three-dimensional (3D) reconstruction was conducted after micro-CT scanning to observe the inner structure of m-HANFs inside the composite hydrogel (Figure S3). The top view clearly showed that in the 5m-HANFs/GelMA group, m-HANFs were scarce and were distributed inhomogeneously, with no stable structure formed. In the 15m- and 25m-HANFs/GelMA groups, m-HANFs both formed network structures, but the network structure in 25m-HANFs/GelMA seemed denser and more inhomogeneous than that of 15m-HANFs/GelMA.

The phase composition of the m-HANFs/GelMA composite hydrogel with different weight fractions of m-HANFs was analyzed by XRD. As shown in Figure 4, 0m-HANFs/GelMA had no typical diffraction peaks. HANFs and m-HANFs had characteristic peaks similar to those of HA standards (JCPDS #09-0432). Notably, compared with each other, the diffraction intensity of HA nanofibers was very sharp at a  $2\theta$  of  $33^\circ$ , which indicated that the HA nanofibers grew preferentially along the c-axis. When it was modified with SBF and incorporated into GelMA, the diffraction peak intensities of m-HANFs/GelMA increased significantly as the weight fraction of m-HANFs increased.

## Mechanical Properties of the m-HANFs/GelMA Composite Hydrogel

Figure 5 showed the stress-strain curves, maximum strain, maximum compressive strength and Young's modulus of the four groups. As shown in Figure 5A, the addition amounts of m-HANFs had a great impact on the mechanical properties of the composite hydrogel. From Figure 5B, we could see that the maximum strain of the m-HANFs/GelMA composite hydrogel showed an upward trend with increasing amounts of m-HANFs, indicating that m-HANFs played an important role in regulating the strain at failure of the composite hydrogel and could enhance its toughness. Figure 5C showed that the maximum stress of the four groups of composite hydrogels increased as the weight fraction of m-HANFs increased except for the 5m-HANFs/GelMA group. On the one hand, this result probably occurred because the added m-HANFs did not homogeneously fill in the whole inner space of the hydrogel when the quantities of m-HANFs were low, which means that m-HANFs cannot form a network structure with low additions of m-HANF, resulting in a weak energy dissipation ability. On the other hand, the inhomogeneous distribution of m-HANFs might affect the photocrosslinking of GelMA, leading to an even lower compressive strength. As the content of m-HANFs increased, they could probably form

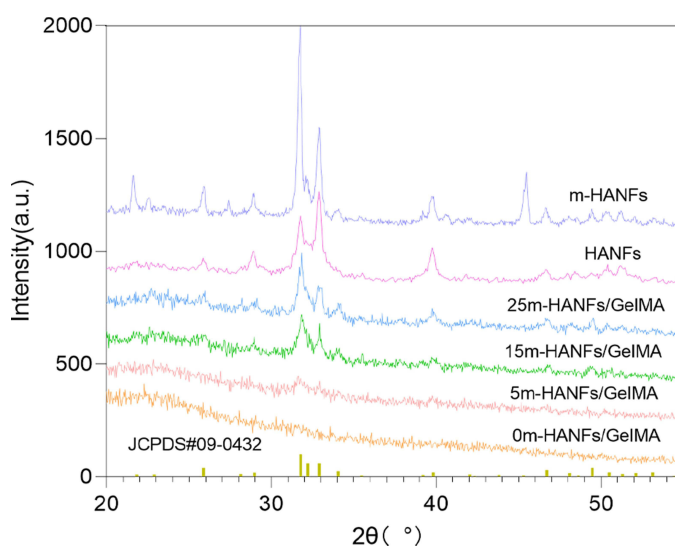


**Figure 4** XRD patterns of HANFs, m-HANFs, and m-HANFs/GelMA with different weight fractions of m-HANFs.

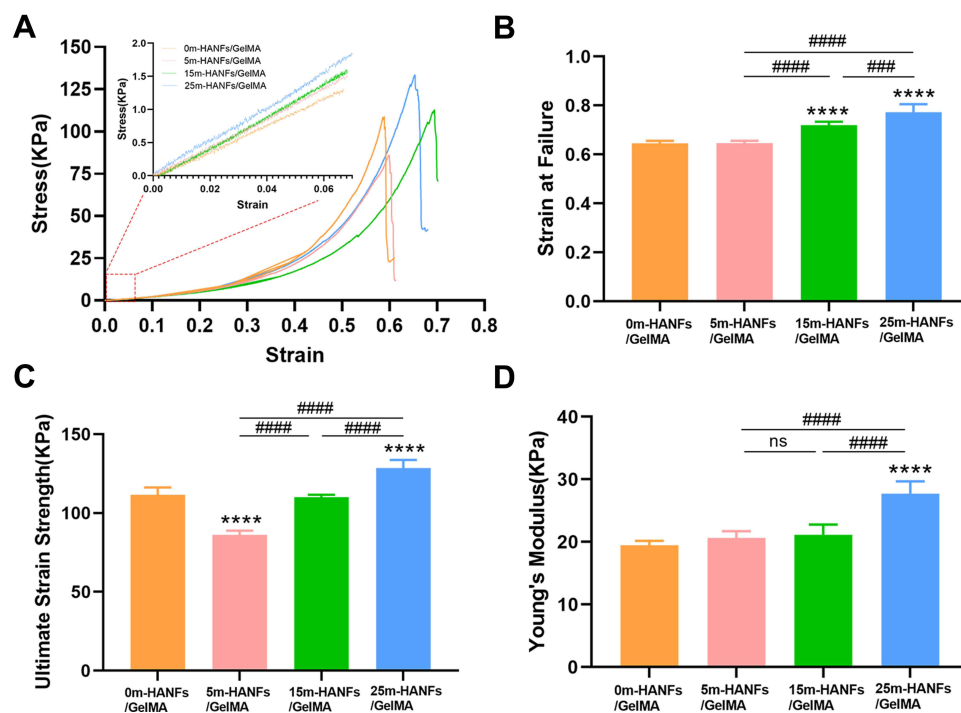


**Figure 5** Mechanical properties of m-HANFs/GelMA hydrogels with different weight fractions of m-HANFs. (A) Stress-strain curves; (B) Strain at failure; (C) Ultimate tensile strength; (D) Young's modulus. Data are presented as the mean  $\pm$  SD ( $n = 6$ ). \*\*\*\* $p < 0.0001$  compared with the 0m-HANFs/GelMA hydrogel. ##### $p < 0.0001$ .

a network structure with enhanced strength to resist external forces. As shown in [Figure 5D](#), the Young's modulus of the m-HANFs/GelMA composite hydrogel showed an upward trend with increasing amounts of m-HANFs, especially the 25m-HANFs/GelMA group, in which the Young's modulus was significantly higher than in the other groups. This result further demonstrated that increased amounts of m-HANFs could form denser networks inside composite hydrogels, which improved their mechanical properties and enhances their energy dissipation ability. These results suggested that the addition of m-HANFs could improve the mechanical properties of GelMA and probably provided more stable support for bone regeneration.

## Swelling Property and Degradation Performance

[Figure 6A](#) shows the swelling ratio profiles of the composite hydrogels. The trend of swelling ratios for samples of the four groups changed to a similar extent. All samples rapidly absorbed water in the initial 1–15 h, and the swelling curve of the samples gradually increased. Notably, the swelling ratios of the composite hydrogels increased with the incorporation of m-HANFs. This was probably due to the fact that the rough and porous m-HANFs incorporated had better hydrophilicity, thus facilitating the diffusion of water molecules into the composite hydrogel. According to the swelling ratio of all groups at 24 h when swelling balances were achieved, we can see that the swelling property did not further increase as the amount of m-HANFs added increased, and the 15m-HANFs/GelMA exhibited higher swelling ratio than 25 m-HANFs/GelMA. This was probably due to m-HANFs forming a denser network structure in 25m-HANFs/GelMA than in 15m-HANFs/GelMA, which hindered their further swelling. The higher swelling capacity of the composite hydrogel reflected its more porous structure, which promoted the exchange of nutrients, metabolic wastes and cell-matrix interactions, ultimately benefiting encapsulated cell survival and reproduction.

[Figure 6B](#) shows the degradation rate profiles of the four groups of composite hydrogels. Generally, hydrogels with higher swelling ratios should have a faster degradation rate. However, interestingly, the m-HANFs/GelMA composite hydrogels we prepared, which had increased swelling properties according to the results above, did not exhibit a faster degradation rate. The results ([Figure 6B](#)) showed that the 0m-HANF/GelMA group had the highest mass loss percentage, which reached 42% on day 56. When the m-HANFs were incorporated, the degradation rate decreased significantly

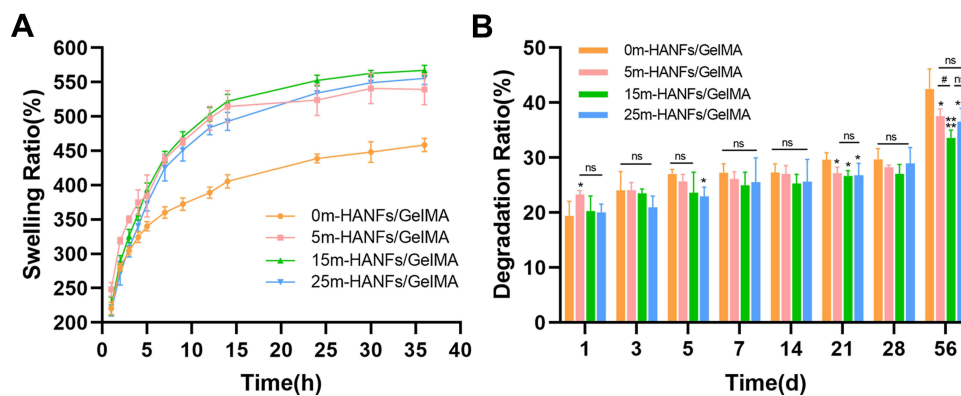


**Figure 6 (A)** Swelling properties and **(B)** degradation performance of m-HANFs/GelMA hydrogels with different weight fractions of m-HANFs vs time. Data are presented as the mean  $\pm$  SD ( $n = 6$ ). \* $p < 0.05$ ; \*\* $p < 0.01$ ; \*\*\* $p < 0.0001$  compared with the 0m-HANFs/GelMA hydrogel. # $p < 0.05$ .

compared with that of the 0m-HANF/GelMA. GelMA is known to degrade faster than crystalline HA,<sup>46</sup> which limits its application in bone regeneration. This result could be explained that the connection between GelMA and m-HANFs could strengthen the structural continuity of GelMA after a long immersion in SBF and thus promoted the overall stability of the composite hydrogel, which, therefore, might be able to provide more sustained support for bone regeneration. In addition, the incorporated m-HANFs with high aspect ratio could form a network structure inside GelMA and protected it from degradation to some extent, even after a long SBF immersion, and thus elevated the stability and integrity of composite hydrogels. Further comparison revealed that the percentage of the mass loss due to degradation in the 15m-HANFs/GelMA group was lower than that of 25m-HANFs/GelMA on days 28 and 56. This can be explained that m-HANFs formed a more uniform network structure in 15m-HANFs/GelMA, which caused them to more strongly combine with GelMA. Meanwhile, the higher amount of m-HANFs in 25m-HANFs/GelMA group led to an inhomogeneous overlap in the m-HANF network structure, and excessive m-HANFs might have weakened their complex with GelMA. Consequently, after soaking for a long time in the SBF, m-HANFs in 25m-HANFs/GelMA tended to be detached from the composite hydrogel more easily, and led to material disintegration.

Gu et al directly incorporated unmineralized HA nanowires (HANWs) into gelatin cryogels to improve their mechanical properties.<sup>47</sup> Their results showed that the swelling ratio of the composite cryogel decreased and the degradation rate increased with the addition of HANWs. Moreover, a deterioration tendency was observed as the amount of HANWs increased, which was not conducive to osteogenesis. Although their results indicated that the composite cryogels exhibited better osteoinductivity in vitro, the same was not further demonstrated in animal experiments, which should be the key for evaluation of the bone regenerative ability of materials. However, in our study, the addition of m-HANFs increased the swelling property of GelMA while decreasing its degradation rate. This might be ascribed to differences in the preparation methods. Gu et al used a quite complicated preparation method for cryogels,<sup>47</sup> but we used the chemical crosslinking method, and the composite hydrogels could be prepared in just one step. The m-HANFs in our study were mineralized in SBF and coated with a layer of biomimetic apatite crystals. This rough and porous layer favored the diffusion of water molecules into the composite hydrogel, thus improving its swelling properties. On the other hand, the rough and porous structure could strengthen the combination inside the composite hydrogel, thus slowing its degradation. However, the sintered unmineralized HANWs reported in the study of Gu et al had smooth surfaces, which probably indicate their weak association with GelMA.<sup>47</sup> Thus, as GelMA gradually degraded, the HANWs precipitated more easily, resulting in faster degradation of the composite hydrogel. In summary, the composite hydrogel prepared in this paper exhibited higher swelling properties and a slower degradation rate than those of previous composite hydrogels, which probably promoted the exchange of nutrients, metabolic wastes and encapsulated cell survival and reproduction, consequently benefiting bone regeneration.

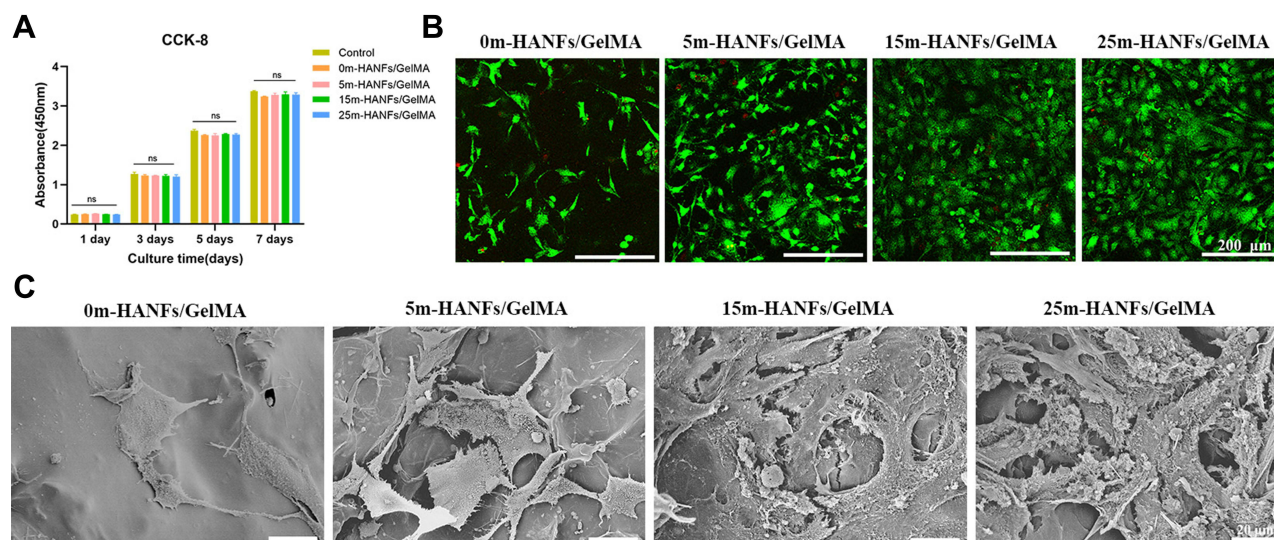


**Figure 7** Biocompatibility of the m-HANFs/GelMA hydrogels. **(A)** Proliferation of MC3T3 cells cocultured with the extracts of m-HANFs/GelMA hydrogels for different time. **(B)** Live/dead cell staining of m-HANFs/GelMA hydrogels with different weight fractions of m-HANFs. Live cells were stained green and dead cells were stained red after 3 days of culture on the hydrogels. **(C)** SEM images of MC3T3 cells on composite hydrogels with different weight fractions of m-HANFs after 3 days of culture. Data are presented as the mean  $\pm$  SD ( $n = 3$ ).

## Cell Viability and Proliferation Assay

Good cytocompatibility is the foundation of biomimetic scaffold materials in tissue engineering. CCK-8 was used to detect the activity of cells cocultured with the extracts of the four composite hydrogel groups at each time point. Compared with the control group, MC3T3 cells (Figure 7A) and rBMSCs (Figure S4) in the four experimental groups did not exhibit significant cell viability differences. Then, live/dead cell staining was carried out to further assess the survival of the cells laden in the composite hydrogels. Observations from the top of the samples revealed many living cells (color green) with different distributions and few dead cells (color red) (Figure 7B). Relatively fewer cells were observed in 0m-HANFs/GelMA and with increasing m-HANF concentration, more green living cells were observed and distributed more broadly in the hydrogels, which might be related to that the rough and porous surface of m-HANFs facilitated cell adhesion and reproduction. Collectively, the results demonstrated that the composite hydrogels had good cytocompatibility, and the addition of m-HANFs was conducive to cell adhesion and growth.

Cell morphology and cytoskeletal organization are important clues that indicate cell homeostasis.<sup>48</sup> The SEM images of the MC3T3-E1 cells that were grown on the composite hydrogels for three days are shown in Figure 7C. In the 0m-HANFs/GelMA group, there were less cells and no evident neurites spreading was observed. In contrast, more cells were observed in the 15 and 25m-HANFs/GelMA groups, and the flattened cells were well-spread with many filopodia, lamellipodia, and cytoplasmic extensions, probably because the rough surface of m-HANFs is more favorable for cell attachment and growth. The relatively smooth surfaces of the 0 and 5m-HANFs/GelMA were unsuitable for cell attachment. This is consistent with the live/dead cell staining results. More elongated cells result in a higher degree of cytoskeletal tension (F-actin filaments) and differential expression of downstream effectors, which could probably enhance pathways associated with osteogenesis.<sup>49,50</sup> In the present study, compared with the other hydrogels, MC3T3-E1 cells in the 15 and 25m-HANFs/GelMA presented a more elongated morphology with evident cytoplasmic extensions, probably suggesting their better cell functionality and osteogenic potential.

## In vitro Osteogenic Differentiation Evaluation

To compare the osteogenic inductive effects of the composite hydrogels on cells, we performed ALP and Alizarin red staining. Alkaline phosphatase activity reflects the early stage of osteogenesis, and alizarin red staining detecting calcium deposition can reflect the late stage of osteogenesis.<sup>51,52</sup> As shown in Figure 8, the lightest staining was observed for the 0m-HANFs/GelMA group, and the staining of the 5, 15, and 25m-HANFs/GelMA gradually deepened with increasing

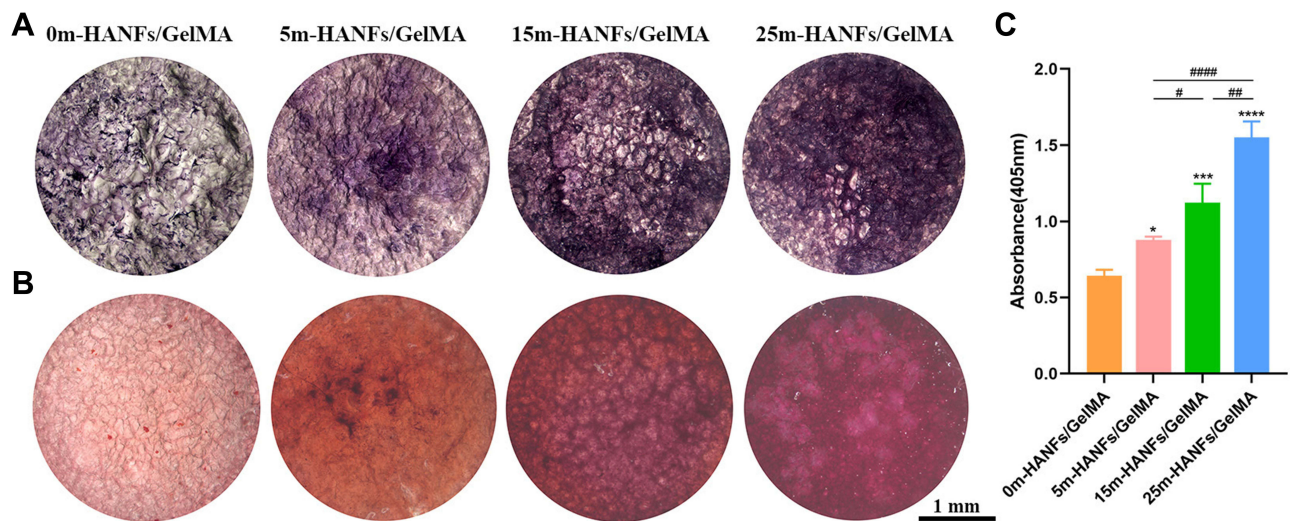


**Figure 8** (A) ALP and (B) alizarin red staining images of MC3T3 cells cultured on m-HANFs/GelMA hydrogels with different m-HANF contents for 7 and 21 days, respectively. (C) Quantification of alizarin red staining. Data are presented as the mean  $\pm$  SD (n = 3). \*p < 0.05; \*\*\*p < 0.001; \*\*\*\*p < 0.0001 compared with the 0m-HANFs/GelMA hydrogel. #p < 0.05; ##p < 0.01; ####p < 0.0001.

m-HANF addition, and the quantitative analysis of alizarin red staining showed the same trend (Figure 8C). The results of rBMSCs presented the similar trends (Figure S5A and B). These results indicated that the addition of m-HANFs enhanced the osteoinductivity of the composite hydrogel, and the effect gradually increased with the increase of added m-HANFs. On one hand, these results could be explained by the observation that the m-HANF we prepared had a bone-like apatite on its surface, which was similar to the inorganic contents of bone tissue, and had good osteoinductivity; on the other hand, as the quantities of m-HANFs increased, the amount of  $\text{Ca}^{2+}$  ions released from the hydrogels increased, promoting cellular osteogenic differentiation and favoring re-deposition of apatite and mineralization.<sup>53</sup>

## In vivo Bone Regeneration Analysis

The obtained results of in vitro experiments showed that the incorporation of m-HANFs modified the physicochemical characteristics of the GelMA-based hydrogel system, which exhibited good biocompatibility and osteoinductivity in

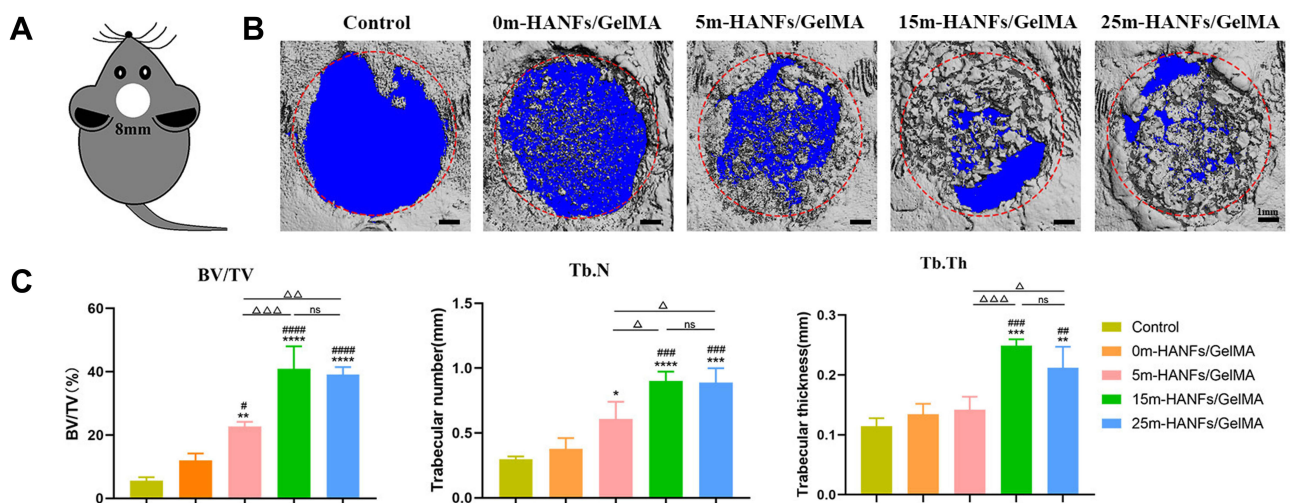


**Figure 9** (A) Schematic diagram of a calvarial defect. (B) Top view of the micro-CT 3D reconstruction of the calvarial defect. (C) Measurement of the bone volume/total volume ratio (BV/TV), trabecular number (Tb.N) and trabecular thickness (Tb.Th). Data are presented as the mean  $\pm$  SD (n = 3). \*p < 0.05; \*\*p < 0.01; \*\*\*p < 0.001; \*\*\*\*p < 0.0001 compared with the control hydrogel. #p < 0.05; ##p < 0.01; ###p < 0.001; ####p < 0.0001 compared with the 0m-HANFs/GelMA hydrogel.  $\Delta$ p < 0.05;  $\Delta\Delta$ p < 0.01;  $\Delta\Delta\Delta$ p < 0.001.

vitro. However, animal experiments are essential for testing the performance of materials before they are applied in the clinic. Hence, we established critical-size calvarial defects in rats (Figure 9A).<sup>54</sup> No obvious weight loss or wound infection was observed after the operation, and the activity of the rats was normal. Twelve weeks after the operation, the skulls were harvested, and bone healing was evaluated with micro-CT, H&E, Masson trichrome and immunohistochemical staining.

First, micro-CT scanning was used to measure the new bone mass and quality in the defects. Figure 9B shows the typical 3D reconstruction figures of calvarial samples, and the defect area is marked by the red circle (8 mm in diameter). The top view clearly shows that all the groups implanted with composite hydrogels displayed more new bone formation than that of the blank group; the 15 and 25m-HANFs/GelMA groups displayed more bone regeneration, and significantly less new bone was observed in the 0 and 5m-HANFs/GelMA. The new bone volume ratio (BV/TV) (Figure 9C) results were basically consistent with the 3D reconstruction figures, while the BV/TV value of the 15m-HANFs/GelMA was slightly higher than that of the 25m-HANFs/GelMA. The trabecular thickness and number are important indexes reflecting the quality of new bone.<sup>55</sup> In Figure 9C, we can see that the measurements of trabecular thickness and number exhibited a similar trend with BV/TV between the groups.

We conducted H&E and Masson's trichrome staining to further evaluate the mass and quality of new bone. The H&E staining (Figure 10) showed that defects in the blank and 0m-HANFs/GelMA groups were mainly filled with granulation tissue. The 5m-HANFs/GelMA exhibited little woven bone formation on the edge of the defect area, while much more new bone formation was observed in the 15 and 25m-HANFs/GelMA groups. In the 25m-HANFs/GelMA group, although some connective tissue remained in the center of the defect area, a bony bridge was almost formed. In addition, some new blood vessels (Figure 10, marked by yellow arrows) could be seen around the newly formed trabeculae in the defect area. Since blood vessels play a vital role in the new bone regeneration process, the occurrence of new blood vessels further indicated excellent ongoing bone remodeling.<sup>56</sup> In the 15m-HANFs/GelMA, bony bridges connecting the defect margins had already formed, and in the new bone area, some mature bone structures could be identified. The cortical-like lamellar bone was combined with the woven bone, and many blood vessels appeared (Figure 10, marked by yellow arrows).

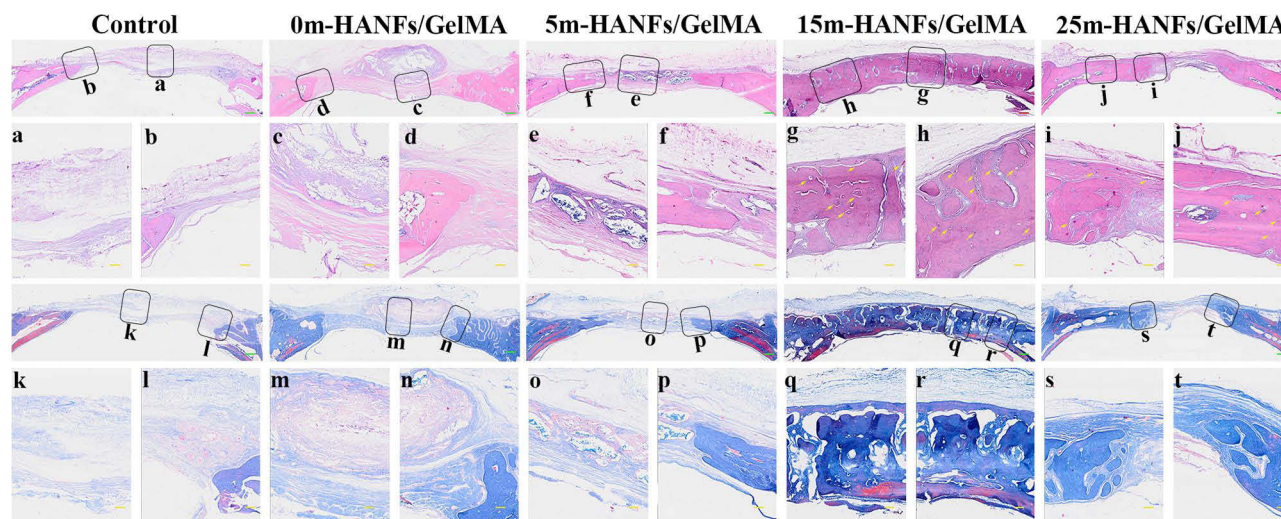


**Figure 10** H&E staining of decalcified sections. a) The middle part of the defect in the control group. b) The margin of the defect in the control group. c) The middle part of the defect in the 0m-HANFs/GelMA group. d) The margin of the defect in the 0m-HANFs/GelMA group. e) The middle part of the defect in the 5m-HANFs/GelMA group. f) The margin of the defect in the 5m-HANFs/GelMA group. g) The middle part of the defect in the 15m-HANFs/GelMA group. h) The margin of the defect in the 15m-HANFs/GelMA group. i) The middle part of the defect in the 25m-HANFs/GelMA group. j) The margin of the defect in the 25m-HANFs/GelMA group. New blood vessels are marked by yellow arrows. Masson's trichrome staining of decalcified sections. k) The middle part of the defect in the control group. l) The margin of the defect in the control group. m) The middle part of the defect in the 0m-HANFs/GelMA group. n) The margin of the defect in the 0m-HANFs/GelMA group. o) The middle part of the defect in the 5m-HANFs/GelMA group. p) The margin of the defect in the 5m-HANFs/GelMA group. q) The middle part of the defect in the 15m-HANFs/GelMA group. r) The margin of the defect in the 15m-HANFs/GelMA group. s) The middle part of the defect in the 25m-HANFs/GelMA group. t) The margin of the defect in the 25m-HANFs/GelMA group. Scale bar: green: 1 mm, yellow: 100  $\mu$ m.

Masson staining can effectively distinguish new and old bone, collagen fibers and muscle fibers according to molecular weight and tissue permeability.<sup>57</sup> Thus, Masson staining was conducted to further confirm new bone formation and maturation (Figure 10). As shown in Figure 10, defects were mainly filled with blue-stained fibrous tissues in the blank, 0 and 5m-HANFs/GelMA groups. In contrast, newly formed woven bone (blue-stained) filled larger areas in the defects in the 15 and 25m-HANFs/GelMA groups than in the other groups. Additionally, more well-arranged bone structures, such as woven bone stained blue and cortical-like lamellar bone stained red, were clearly observed in the 15m-HANFs/GelMA, indicating that it was at the late stage of osteogenesis, which was consistent with the results of H&E staining.

The immunohistochemical staining images of Runx2, Col1a1 and OCN are shown in Figure 11. Runx2 is a key transcriptional regulator of osteogenic differentiation that directly and indirectly modulates the expression of osteoblast-specific genes.<sup>58</sup> More Runx2 proteins were expressed in the 15 and 25m-HANFs/GelMA groups than in the other groups, especially in the 15m-HANFs/GelMA group. Col1a1 is a major constituent of the organic extracellular matrix of bone tissue, and its expression has been found to occur at high levels during the early stages of osteogenesis,<sup>59,60</sup> thus, Col1a1 is considered an early osteogenic marker. The results showed higher Col1a1 expression in the blank and 0m-HANFs/GelMA groups than in the other groups, indicating that these groups were still in the early stages of osteogenesis. OCN encodes a major noncollagenous protein of the extracellular matrix and is regarded as a late marker of the osteogenic differentiation pathway.<sup>61</sup> A higher level of OCN expression was observed in the 15 and 25m-HANFs/GelMA groups than in the other groups, which is thought to be associated with the osteoblastic populations of these two groups having better maturation and differentiation properties.<sup>62,63</sup>

In this study, we successfully prepared HANFs with ultrahigh aspect ratio and mineralized them in SBF to make their surfaces coated with bone-like apatite that simulated the natural bone apatite in structure and composition. Then, different amounts of biomimetic m-HANFs were incorporated into GelMA to form m-HANFs/GelMA composite hydrogels. The results showed that the incorporation of m-HANFs successfully improved the mechanical, swelling, degradation properties and bone regenerative ability of GelMA. However, the physicochemical and bone regenerative performances of the composite hydrogels did not continuously increase as the content of m-HANFs increased. Although 25m-HANFs/GelMA exhibited better mechanical properties and osteoinductivity in vitro, 15m-HANFs/GelMA displayed better swelling and degradation performances and a better bone repair effect in vivo, which was probably related to the structure of m-HANFs inside the hydrogel. As shown in Figure S3, the m-HANFs in the 25m-HANFs/GelMA exhibited a dense and inhomogeneous network structure, which probably exerted a negative impact not only on the swelling and degradation performances but also on cell migration, growth and the exchange of nutrients and metabolic wastes. By contrast, 15m-HANFs/GelMA presented a relatively more uniform and stable network, and they had higher swelling

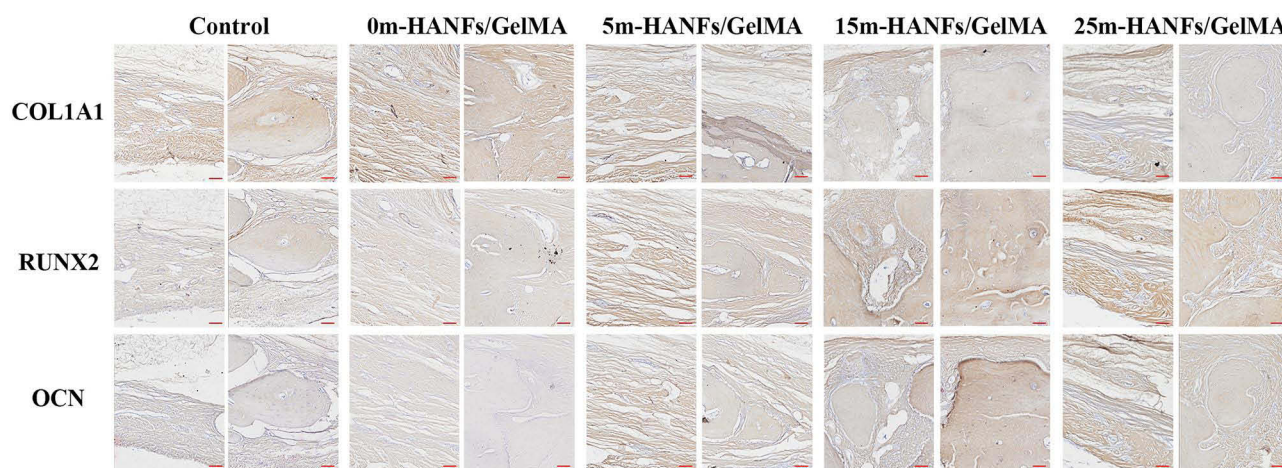


**Figure 11** Immunohistochemical staining of Runx2, Col1a1, and OCN (brown). Scale bar: 50  $\mu$ m.

rates and prolonged degradation, thus favoring cell growth and providing more stable support for bone regeneration *in vivo*.

The results of our *in vitro* osteoinduction experiments were not exactly consistent with our *in vivo* experiments, probably because cells were mainly seeded and incubated on the surface layer of the composite hydrogel due to short-term culture *in vitro*, while in the repair process of calvarial defects, cells grew and differentiated inside the hydrogel, thus probably being more influenced by the inner network structure of the composite hydrogel. A previous study reported that a gelatin cryogel exhibited constantly increasing osteoinductivity *in vitro* as the content of unmineralized HANWs increased, but the same result was not demonstrated *in vivo*.<sup>47</sup> Thus, the data could not reflect the actual bone regenerative ability of the composite hydrogel.

*In vivo* bone regeneration, unlike *in vitro* short-term osteogenic induction, occurs in a more complex environment, which is influenced by various factors, including more complicated cell sources, mesenchymal stem cell recruitment and further differentiation, and angiogenesis. Moreover, *in vivo* bone regeneration involves the connection and reconstitution of the original and new bones, rather than merely new bone regeneration. Barros et al studied the influence of the HANP content (30 to 70 wt%) on alginate-based hydrogels to evaluate the best formulation for maximizing bone tissue regeneration.<sup>42</sup> Their results also showed that the bone regenerative effect of the composite hydrogel did not continuously increase as the content of HANPs increased. The hydrogel with a 30% HANP content exhibited higher expression of osteogenic transcription factors and higher collagenous deposition, trabecular bone formation and matrix mineralization than hydrogels with higher HANP contents (50 and 70%). This was probably related to the optimal concentration of  $\text{Ca}^{2+}$  ions released from composites because of the degradation of incorporated minerals.<sup>42,64</sup> Some studies have reported that  $\text{Ca}^{2+}$  ions released from composites, though regarded as an osteoinductive factor, can, to some extent, affect the metabolism of osteoblasts and bone remodeling within the implantation site; in addition, long exposure to an environment with an excessively high concentration of  $\text{Ca}^{2+}$  ions might exert a negative effect on bone regeneration.<sup>42,65</sup> Therefore, a higher content of inorganic mineral fillers does not necessarily suggest a better bone regenerative ability of composite hydrogels.

In this study, we found that the addition of m-HANFs played a very important role in the physico-chemical properties and osteoinductivity of the composite hydrogel. However, the bone regenerative capacity of the composite hydrogel did not continuously increase as the content of m-HANFs increased. In particular, 15m-HANFs/GelMA formed a more uniform network inside the composite hydrogel and exhibited higher swelling rates, prolonged degradation, and the best bone regenerative effect *in vivo*. Therefore, the proportion of m-HANFs and GelMA needs to be further optimized to better promote bone tissue regeneration.

## Conclusion

In this study, we successfully prepared HANFs with ultrahigh aspect ratio and mineralized them in SBF to make their surfaces coated with bone-like apatite. The trace element doped biomimetic apatite mineral layer on the m-HANFs' surfaces simulated the natural bone apatite in structure and composition and was beneficial for bone regeneration. Different amounts of biomimetic m-HANFs were incorporated into GelMA to form m-HANFs/GelMA composite hydrogels. The results indicated that the addition of biomimetic m-HANFs improved the mechanical and swelling properties and degradation and osteoinductive performance of GelMA; however, the performance improvement of the composite hydrogel did not continuously increase as the content of m-HANFs increased. Collectively, 15m-HANFs/GelMA exhibited the best swelling and degradation performances and the best bone repair effect *in vivo*. Therefore, biomimetic m-HANFs/GelMA hydrogel may provide a novel option for bone tissue engineering in the future. More investigations are needed to further optimize the proportion of m-HANFs and GelMA for improving their bone repair effect.

## Acknowledgments

This work was supported by the Natural Science Foundation Project of CQ (Grant Nos. cstc2021jcyj-msxmX0360 and cstc2021jcyj-msxmX0707), National Natural Science Foundation of China (Grant Nos. 81771082 and 31971282), Chongqing Graduate Tutor Team (2019) (Grant No. dstd201903) and the Postgraduate Students' Innovative Research and Development Projects of Chongqing (Grant No. CYB19158).

## Disclosure

The authors report no conflicts of interest in this work.

## References

1. Li Z, Du T, Ruan C, Niu X. Bioinspired mineralized collagen scaffolds for bone tissue engineering. *Bioact Mater.* 2021;6(5):1491–1511. doi:10.1016/j.bioactmat.2020.11.004
2. Ovsianikov A, Khademhosseini A, Mironov V. The synergy of scaffold-based and scaffold-free tissue engineering strategies. *Trends Biotechnol.* 2018;36(4):348–357. doi:10.1016/j.tibtech.2018.01.005
3. Du T, Niu X, Hou S, et al. Highly aligned hierarchical intrafibrillar mineralization of collagen induced by periodic fluid shear stress. *J Mater Chem B.* 2020;8(13):2562–2572. doi:10.1039/C9TB02643F
4. Zhang X, Li Z, Yang P, et al. Polyphenol scaffolds in tissue engineering. *Mater Horiz.* 2021;8(1):145–167. doi:10.1039/D0MH01317J
5. Fernandez-Yague M, Abbah S, McNamara L, et al. Biomimetic approaches in bone tissue engineering: integrating biological and physicomachanical strategies. *Adv Drug Deliver Rev.* 2015;84:1–29.
6. Wei W, Ma Y, Yao X, et al. Advanced hydrogels for the repair of cartilage defects and regeneration. *Bioact Mater.* 2021;6(4):998–1011. doi:10.1016/j.bioactmat.2020.09.030
7. Eggermont LJ, Rogers ZJ, Colombani T, Memic A, Bencherif SA. Injectable cryogels for biomedical applications. *Trends Biotechnol.* 2020;38(4):418–431. doi:10.1016/j.tibtech.2019.09.008
8. Li Y, Yang H, Lee D. Advances in biodegradable and injectable hydrogels for Biomedical applications. *J Control Release.* 2021;330:151–160. doi:10.1016/j.jconrel.2020.12.008
9. Maturavongsadit P, Bi X, Metavarayuth K, Luckanagul J, Wang Q. Influence of cross-linkers on the in vitro chondrogenesis of mesenchymal stem cells in hyaluronic acid hydrogels. *ACS Appl Mater Interfaces.* 2017;9(4):3318–3329. doi:10.1021/acsami.6b12437
10. Zhu H, Monavari M, Zheng K, et al. 3D bioprinting of multifunctional dynamic nanocomposite bioinks incorporating Cu-doped mesoporous bioactive glass nanoparticles for bone tissue engineering. *Small.* 2022;e2104996. doi:10.1002/sml.202104996
11. Lee C-S, Hwang HS, Kim S, et al. Inspired by nature: facile design of nanoclay-organic hydrogel bone sealant with multifunctional properties for robust bone regeneration. *Adv Funct Mater.* 2020;30(43):2003717. doi:10.1002/adfm.202003717
12. Yue K, Trujillo-de Santiago G, Alvarez MM, et al. Synthesis, properties, and biomedical applications of gelatin methacryloyl (GelMA) hydrogels. *Biomaterials.* 2015;73:254–271. doi:10.1016/j.biomaterials.2015.08.045
13. Xu J, Feng Q, Lin S, et al. Injectable stem cell-laden supramolecular hydrogels enhance in situ osteochondral regeneration via the sustained co-delivery of hydrophilic and hydrophobic chondrogenic molecules. *Biomaterials.* 2019;210:51–61. doi:10.1016/j.biomaterials.2019.04.031
14. Deng Z, Guo Y, Ma P, Guo B. Rapid thermal responsive conductive hybrid cryogels with shape memory properties, photothermal properties and pressure dependent conductivity. *J Colloid Interf Sci.* 2018;526:281–294. doi:10.1016/j.jcis.2018.04.093
15. Zhu J. Bioactive modification of poly(ethylene glycol) hydrogels for tissue engineering. *Biomaterials.* 2010;31(17):4639–4656. doi:10.1016/j.biomaterials.2010.02.044
16. Chen X, Tan B, Bao Z, et al. Enhanced bone regeneration via spatiotemporal and controlled delivery of a genetically engineered BMP-2 in a composite hydrogel. *Biomaterials.* 2021;277:121117. doi:10.1016/j.biomaterials.2021.121117
17. Kurian AG, Singh RK, Patel KD, Lee J-H, Kim H-W. Multifunctional GelMA platforms with nanomaterials for advanced tissue therapeutics. *Bioact Mater.* 2022;8:267–295. doi:10.1016/j.bioactmat.2021.06.027
18. Klotz BJ, Gawlitta D, Rosenberg AJ, Malda J, Melchels FPW. Gelatin-methacryloyl hydrogels: towards biofabrication-based tissue repair. *Trends Biotechnol.* 2016;34(5):394–407. doi:10.1016/j.tibtech.2016.01.002
19. Yang F, Niu X, Gu X, et al. Biodegradable magnesium-incorporated Poly(l-lactic acid) microspheres for manipulation of drug release and alleviation of inflammatory response. *ACS Appl Mater Interfaces.* 2019;11(26):23546–23557. doi:10.1021/acsami.9b03766
20. Huang B, Chen M, Tian J, et al. Oxygen-carrying and antibacterial fluorinated nano-hydroxyapatite incorporated hydrogels for enhanced bone regeneration. *Adv Healthc Mater.* 2022;e2102540. doi:10.1002/adhm.202102540
21. Shi Z, Zhong Q, Chen Y, et al. Nanohydroxyapatite, nanosilicate-reinforced injectable, and biomimetic gelatin-methacryloyl hydrogel for bone tissue engineering. *Int J Nanomedicine.* 2021;16:5603–5619. doi:10.2147/IJN.S321387
22. Xu Y, Gaille MP, Zheng K, et al. A self-assembled matrix system for cell-bioengineering applications in different dimensions, scales, and geometries. *Small.* 2022;e2104758. doi:10.1002/sml.202104758
23. Brunello G, Sivolella S, Meneghello R, et al. Powder-based 3D printing for bone tissue engineering. *Biotechnol Adv.* 2016;34(5):740–753. doi:10.1016/j.biotechadv.2016.03.009
24. Ingavle GC, Gionet-Gonzales M, Vorwald CE, et al. Injectable mineralized microsphere-loaded composite hydrogels for bone repair in a sheep bone defect model. *Biomaterials.* 2019;197:119–128. doi:10.1016/j.biomaterials.2019.01.005
25. Raina D, Isaksson H, Teotia A, et al. Biocomposite macroporous cryogels as potential carrier scaffolds for bone active agents augmenting bone regeneration. *J Control Release.* 2016;235:365–378. doi:10.1016/j.jconrel.2016.05.061
26. Thoniyot P, Tan M, Karim A, Young D, Loh X. Nanoparticle-hydrogel composites: concept, design, and applications of these promising, multifunctional materials. *Adv Sci.* 2015;2:1400010. doi:10.1002/advs.201400010
27. Sun T, Yu W, Zhu Y, et al. Porous nanocomposite comprising ultralong hydroxyapatite nanowires decorated with zinc-containing nanoparticles and chitosan: synthesis and application in bone defect repair. *Chemistry.* 2018;24(35):8809–8821. doi:10.1002/chem.201800425
28. Huang G, Yu H, Wang X, et al. Highly porous and elastic aerogel based on ultralong hydroxyapatite nanowires for high-performance bone regeneration and neovascularization. *J Mater Chem B.* 2021;9(5):1277–1287. doi:10.1039/D0TB02288H
29. Cho K, Wang G, Raju R, et al. Influence of surface treatment on the interfacial and mechanical properties of short S-glass fiber-reinforced dental composites. *ACS Appl Mater Interfaces.* 2019;11(35):32328–32338. doi:10.1021/acsami.9b01857
30. Santos A, Ferreira C, Veiga F, et al. Halloysite clay nanotubes for life sciences applications: from drug encapsulation to bioscaffold. *Adv Colloid Interf Sci.* 2018;257:58–70. doi:10.1016/j.cis.2018.05.007

31. Farokhi M, Mottaghtalab F, Samani S, et al. Silk fibroin/hydroxyapatite composites for bone tissue engineering. *Biotechnol Adv.* 2018;36(1):68–91. doi:10.1016/j.biotechadv.2017.10.001
32. Liao S, Wang W, Uo M, et al. A three-layered nano-carbonated hydroxyapatite/collagen/PLGA composite membrane for guided tissue regeneration. *Biomaterials.* 2005;26(36):7564–7571. doi:10.1016/j.biomaterials.2005.05.050
33. Kim H, Kim H, Salih V. Stimulation of osteoblast responses to biomimetic nanocomposites of gelatin-hydroxyapatite for tissue engineering scaffolds. *Biomaterials.* 2005;26(25):5221–5230. doi:10.1016/j.biomaterials.2005.01.047
34. Fleet ME, Liu X. Coupled substitution of type A and B carbonate in sodium-bearing apatite. *Biomaterials.* 2007;28(6):916–926. doi:10.1016/j.biomaterials.2006.11.003
35. Sun T, Zhu Y, Chen F. Highly flexible multifunctional biopaper comprising chitosan reinforced by ultralong hydroxyapatite nanowires. *Chemistry.* 2017;23(16):3850–3862. doi:10.1002/chem.201605165
36. Kokubo T, Takadama H. How useful is SBF in predicting in vivo bone bioactivity? *Biomaterials.* 2006;27(15):2907–2915. doi:10.1016/j.biomaterials.2006.01.017
37. Xiao W, Qu X, Tan Y, et al. Synthesis of photocrosslinkable hydrogels for engineering three-dimensional vascular-like constructs by surface tension-driven assembly. *Mater Sci Eng C Mater Biol Appl.* 2020;116:111143. doi:10.1016/j.msec.2020.111143
38. Eke G, Mangir N, Hasirci N, MacNeil S, Hasirci V. Development of a UV crosslinked biodegradable hydrogel containing adipose derived stem cells to promote vascularization for skin wounds and tissue engineering. *Biomaterials.* 2017;129:188–198. doi:10.1016/j.biomaterials.2017.03.021
39. Nichol JW, Koshy ST, Bae H, et al. Cell-laden microengineered gelatin methacrylate hydrogels. *Biomaterials.* 2010;31(21):5536–5544. doi:10.1016/j.biomaterials.2010.03.064
40. Fang J, Li P, Lu X, et al. A strong, tough, and osteoconductive hydroxyapatite mineralized polyacrylamide/dextran hydrogel for bone tissue regeneration. *Acta Biomater.* 2019;88:503–513. doi:10.1016/j.actbio.2019.02.019
41. Zhang X, Chang W, Lee P, et al. Polymer-ceramic spiral structured scaffolds for bone tissue engineering: effect of hydroxyapatite composition on human fetal osteoblasts. *PLoS One.* 2014;9(1):e85871. doi:10.1371/journal.pone.0085871
42. Barros J, Ferraz MP, Azeredo J, et al. Alginate-nanohydroxyapatite hydrogel system: optimizing the formulation for enhanced bone regeneration. *Mater Sci Eng C Mater Biol Appl.* 2019;105:109985. doi:10.1016/j.msec.2019.109985
43. Costa DO, Prowse PDH, Chrones T, et al. The differential regulation of osteoblast and osteoclast activity by surface topography of hydroxyapatite coatings. *Biomaterials.* 2013;34(30):7215–7226. doi:10.1016/j.biomaterials.2013.06.014
44. Gentile F, Tirinato L, Battista E, et al. Cells preferentially grow on rough substrates. *Biomaterials.* 2010;31(28):7205–7212. doi:10.1016/j.biomaterials.2010.06.016
45. Annabi N, Nichol JW, Zhong X, et al. Controlling the porosity and microarchitecture of hydrogels for tissue engineering. *Tissue Eng Part B Rev.* 2010;16(4):371–383. doi:10.1089/ten.teb.2009.0639
46. Yang G, Liu H, Hu X, et al. Bio-inspired hybrid nanoparticles promote vascularized bone regeneration in a morphology-dependent manner. *Nanoscale.* 2017;9(18):5794–5805. doi:10.1039/C7NR00347A
47. Gu L, Zhang J, Li L, et al. Hydroxyapatite nanowire composited gelatin cryogel with improved mechanical properties and cell migration for bone regeneration. *Biomed Mater.* 2019;14(4):045001. doi:10.1088/1748-605X/ab1583
48. Cabezas MD, Meckes B, Mirkin CA, Mrksich M. Subcellular control over focal adhesion anisotropy, independent of cell morphology, dictates stem cell fate. *ACS Nano.* 2019;13(10):11144–11152. doi:10.1021/acsnano.9b03937
49. Li YY, Choy TH, Ho FC, Chan PB. Scaffold composition affects cytoskeleton organization, cell-matrix interaction and the cellular fate of human mesenchymal stem cells upon chondrogenic differentiation. *Biomaterials.* 2015;52:208–220. doi:10.1016/j.biomaterials.2015.02.037
50. Zhao R, Xie P, Zhang K, et al. Selective effect of hydroxyapatite nanoparticles on osteoporotic and healthy bone formation correlates with intracellular calcium homeostasis regulation. *Acta Biomater.* 2017;59:338–350. doi:10.1016/j.actbio.2017.07.009
51. Lee SS, Kim JH, Jeong J, et al. Sequential growth factor releasing double cryogel system for enhanced bone regeneration. *Biomaterials.* 2020;257:120223. doi:10.1016/j.biomaterials.2020.120223
52. Yuan Z, Tao B, He Y, et al. Remote eradication of biofilm on titanium implant via near-infrared light triggered photothermal/photodynamic therapy strategy. *Biomaterials.* 2019;223:119479. doi:10.1016/j.biomaterials.2019.119479
53. Dhivya S, Saravanan S, Sastry TP, Selvamurugan N. Nanohydroxyapatite-reinforced chitosan composite hydrogel for bone tissue repair in vitro and in vivo. *J NanobioTechnology.* 2015;13:40. doi:10.1186/s12951-015-0099-z
54. Spicer PP, Kretlow JD, Young S, et al. Evaluation of bone regeneration using the rat critical size calvarial defect. *Nat Protoc.* 2012;7(10):1918–1929. doi:10.1038/nprot.2012.113
55. Lin Z, Wu J, Qiao W, et al. Precisely controlled delivery of magnesium ions thru sponge-like monodisperse PLGA/nano-MgO-alginate core-shell microsphere device to enable in-situ bone regeneration. *Biomaterials.* 2018;174:1–16. doi:10.1016/j.biomaterials.2018.05.011
56. Han H-S, Jun I, Seok H-K, et al. Biodegradable magnesium alloys promote angio-osteogenesis to enhance bone repair. *Adv Sci.* 2020;7(15):2000800. doi:10.1002/advs.202000800
57. Chen JL, Yin Z, Shen WL, et al. Efficacy of hESC-MSCs in knitted silk-collagen scaffold for tendon tissue engineering and their roles. *Biomaterials.* 2010;31(36):9438–9451. doi:10.1016/j.biomaterials.2010.08.011
58. Kang H, Wong DSH, Yan X, et al. Remote control of multimodal nanoscale ligand oscillations regulates stem cell adhesion and differentiation. *ACS Nano.* 2017;11(10):9636–9649. doi:10.1021/acsnano.7b02857
59. Black C, Kanczler JM, de Andrés MC, et al. Characterisation and evaluation of the regenerative capacity of Stro-4+ enriched bone marrow mesenchymal stromal cells using bovine extracellular matrix hydrogel and a novel biocompatible melt electro-written medical-grade polycaprolactone scaffold. *Biomaterials.* 2020;247:119998. doi:10.1016/j.biomaterials.2020.119998
60. Yu L, Sui B, Fan W, et al. Exosomes derived from osteogenic tumor activate osteoclast differentiation and concurrently inhibit osteogenesis by transferring COL1A1-targeting miRNA-92a-1-5p. *J Extracell Vesicles.* 2021;10(3):e12056. doi:10.1002/jev2.12056
61. Wang R, Shi M, Xu F, et al. Graphdiyne-modified TiO<sub>2</sub> nanofibers with osteoinductive and enhanced photocatalytic antibacterial activities to prevent implant infection. *Nat Commun.* 2020;11(1):4465. doi:10.1038/s41467-020-18267-1

62. Lee N-H, Kang MS, Kim T-H, et al. Dual actions of osteoclastic-inhibition and osteogenic-stimulation through strontium-releasing bioactive nanoscale cement imply biomaterial-enabled osteoporosis therapy. *Biomaterials*. 2021;276:121025. doi:10.1016/j.biomaterials.2021.121025
63. Mota C, Camarero-Espinosa S, Baker MB, Wieringa P, Moroni L. Bioprinting: from tissue and organ development to models. *Chem Rev*. 2020;120(19):10547–10607. doi:10.1021/acs.chemrev.9b00789
64. Gu H, Guo F, Zhou X, et al. The stimulation of osteogenic differentiation of human adipose-derived stem cells by ionic products from akermanite dissolution via activation of the ERK pathway. *Biomaterials*. 2011;32(29):7023–7033. doi:10.1016/j.biomaterials.2011.06.003
65. Chan G, Mooney DJ. Ca(2+) released from calcium alginate gels can promote inflammatory responses in vitro and in vivo. *Acta Biomater*. 2013;9(12):9281–9291. doi:10.1016/j.actbio.2013.08.002

International Journal of Nanomedicine

Dovepress

## Publish your work in this journal

The International Journal of Nanomedicine is an international, peer-reviewed journal focusing on the application of nanotechnology in diagnostics, therapeutics, and drug delivery systems throughout the biomedical field. This journal is indexed on PubMed Central, MedLine, CAS, SciSearch®, Current Contents®/Clinical Medicine, Journal Citation Reports/Science Edition, EMBase, Scopus and the Elsevier Bibliographic databases. The manuscript management system is completely online and includes a very quick and fair peer-review system, which is all easy to use. Visit <http://www.dovepress.com/testimonials.php> to read real quotes from published authors.

Submit your manuscript here: <https://www.dovepress.com/international-journal-of-nanomedicine-journal>